# Numerical Investigation of Air Pumping Noise Generation in a 3D Tire Geometry

#### **Prashanta Gautam**

Graduate Research Assistant
Department of Mechanical Engineering
University of Akron
Akron, Ohio 44325
Email: pg37@zips.uakron.edu

Abhilash J. Chandy \*

Associate Professor
Department of Mechanical Engineering
University of Akron
Akron, Ohio 44325
Email: achandy@uakron.edu

## **ABSTRACT**

Tire noise reduction is an important aspect of overall vehicle noise reduction. However, due to the complex nature of tire noise generation and interrelation between various generation mechanisms, it is difficult to isolate, predict and control tire noise. Aerodynamic noise generation mechanisms in tires are difficult to predict experimentally, resulting in the need for an accurate numerical model. Computational fluid dynamics (CFD) is used here to propose a computational model capable of predicting air-pumping noise generation. Groove deformations are prescribed by custom functions instead of using structural solvers and the rotation of tire is represented by using mesh motion and deformation techniques. Near-field and far-field acoustic characteristics are predicted using fluid dynamic equations and acoustic models. The use of various spectral analysis tools show that the proposed model is capable of predicting the high frequency air-pumping noise while also predicting other aerodynamic mechanisms such as pipe resonance, Helmholtz resonance and rotational turbulence. This study is intended to provide an understanding of the various aerodynamic noise generation mechanisms so that numerical models can be used in the future to predict tire acoustics economically and effectively.

#### 1 Introduction

A significant contribution to noise pollution in urban areas results from traffic noise. While the main contribution to traffic noise is from the vehicle engine and powertrain [1], tire noise is critical to vehicle noise control. This is due to the difficulty in attenuating tire noise, after it is generated at the source [2]. Furthermore, with the reduction in engine noise and introduction of electric vehicles, which have no engines and hence, no engine noise, the contribution of tire noise to the overall vehicle noise has increased. Tire/pavement noise represents 75% to 90% of the total noise in passenger vehicles while it could be just as significant in other large vehicles [3]. Consequently, there is an increased need to investigate and control tire noise.

Tire noise generation is a complicated phenomenon and there are various mechanisms involved, that produce a combined effect on the overall noise generation process. While it is difficult to isolate and independently study the contribution of each mechanism, they can be roughly classified into generation mechanisms and amplification/reduction mechanisms [4,5]. Tire noise generation mechanisms can be further classified into mechanical and aerodynamic types. While the mechanical kind are caused by low frequency structural vibrations in the tire, the aerodynamic ones are caused by the air-flow and corresponding high frequency pressure changes in the surrounding, due to the motion of the tire and treads. The amplification mechanisms

<sup>\*</sup>Corresponding author

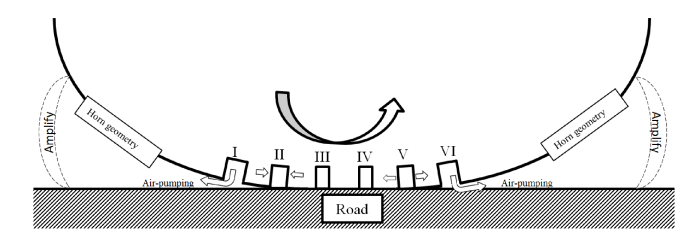


Fig. 1: Schematic diagram showing different stages of deformation of a transverse tire groove during tire/road interaction of a rotating tire.

are responsible for the modification of the structural and aerodynamic noise generated in tires. Horn effect is an important amplification mechanism in tires, due to the presence of horn-like geometries between the tire belt and the road. These geometries amplify sound mainly in the upstream and downstream sides of the tire [6] and the amplifications could be as high as 10-20 dB [6,7].

The various challenges associated with conducting experiments related to tire noise have limited the number of studies investigating aerodynamic tire noise generation mechanisms. Specifically, operating conditions and background noise need to be carefully managed and in addition, the airborne noise needs to be isolated from the structure-borne noise in a tire/road noise experiment, thereby making the analysis much more complicated. As an alternative analysis tool, numerical modeling can investigate aerodynamic tire noise and the influence of several parameters on it, with relative ease. However, challenges associated with developing a computational model are mainly related to the complex and nonlinear nature of the interaction between structural deformation and aerodynamic mechanisms. The use of a fluid-structure interaction (FSI) solver to analyze aerodynamic noise generation mechanisms has proven to be challenging and a numerical model capable of combining the tire structural dynamics and aerodynamics as a whole is yet to be developed [8].

Although, simplified numerical models have been proposed for the study of aerodynamic mechanisms such as air-pumping [9–12]. Air-pumping is an aerodynamic noise generation mechanism caused due to the displacement of air from pockets in tires and/or the road surface [13]. While the previously-proposed air-pumping models ranged from the usage of the acoustic monopole assumption [9] to wave equations which take into account the non-linear nature of air [10,11], these models deal with the fundamental aspects of air-pumping and are not practically applicable in tire/road interactions.

The three-stage hybrid technique proposed by [12] is a more practical numerical model and it used a piston/sliding-door/cavity system to predict air-pumping in actual tire geometries. However, while the model is able to take into account the non-linearity associated with air-pumping, the effect of rotation of the tire on the small scale noise generation was not considered directly. A new and more straightforward methodology that matches more realistic tire rotation and deformation scenarios is proposed in this paper and its effectiveness is analyzed for a 3-dimensional tire geometry.

In this paper, a 3-dimensional analysis of the air-pumping noise generation mechanism is carried out using the commercial code, ANSYS Fluent. The use of a structural solver is circumvented through the *apriori* specification of groove deformations, whose values are obtained from experimental observations. Thus, this technique does ignore the nonlinear properties of the tire material. However, such a methodology, with its relative less computational expense is a first step towards investigating aerodynamic noise generation mechanisms in tires and can provide valuable insights into the process. For the near-field, a solution of the fluid dynamics equations are obtained using a large eddy simulation (LES)-based turbulence modeling approach to resolve the large scales associated with rotational turbulence and the flow dynamics of air. The flow variables in the near-field domain are used to predict the far-field acoustic pressure using the Ffowcs-Williams and Hawkings (FW-H) acoustic model. The resulting pressure waves are analyzed at various near-field and far-field receiver locations and the acoustic characteristics are studied using various tools and techniques. Validation of the results is performed using empirical relations, qualitative comparisons with past studies and mesh independence studies.

#### 2 Tire rotation model

This section describes the tire rotation and deformation model employed in this study. Figure 1 shows the twodimensional schematic representation of different stages of the deformation of the transverse tire grooves in a tire during its rotation and interaction with the road surface. The illustrated model is implemented to obtain a near-field fluid dynamic solution and related acoustics, while an acoustic model is used to predict far-field acoustic characteristics. A control surface is used to generate input for the far-field acoustic model and the solution for all receiver locations are obtained through a single simulation. The resulting computational model is intended to closely represent an experimental setup, where a tire is rotating over a smooth drum at a typical operating velocity inside a semi-anechoic chamber [14].

The deformation of the groove is characterized in six stages. In stage I, the groove is on the upstream side of the tire, as it is approaching the tire/road interface, and as this happens, the groove undergoes deformation in stage II, causing pressure waves to propagate through the horn geometry of the tire. In stage III, the groove is completely in contact with the ground

and moving along the contact patch, until stage IV. The groove approaches the downstream side of the tire in stage V, where it undergoes a volume increase as it leaves the contact patch and creates pressure waves which propagate through the horn geometry on the downstream side of the tire. In stage VI, the groove is clear of the contact patch and returns back to its original shape.

A previous unpublished study by the authors had used a two-dimensional version of the same model. A distinction of the current model from its two-dimensional counterpart is that for stages III and IV in the 2D model, the air trapped inside the grooves are not able to escape through the sides of the tire, due to the absence of the third dimension, and therefore, would be released only on the downstream side. This produces larger pressure waves than expected and consequently, higher sound pressure levels. Furthermore, pipe resonance effects are not captured. A three-dimensional consideration overcomes this problem as the trapped air may leak through the groove openings on the sides and traverse through the horn geometry, producing a more realistic effect. Consequently, a three-dimensional consideration is also capable of accounting for pipe resonance effects, as the groove moves through the contact patch.

## 3 Governing equations

The governing equations solved in the simulations presented here involve the near-field fluid dynamics, far-field acoustics and the spectral analysis of the acoustic data.

## 3.1 Navier-Stokes equations

Since the objective of this paper is to investigate aerodynamic noise, it is necessary to take into account the compressible nature of air in order to capture acoustic wave generation and propagation accurately, although the changes in density are not very large. Consequently, the solution for the fluid domain in the near-field is obtained using the compressible Navier-Stokes equations. The continuity and momentum equations are formulated in Equations (1) and (2), respectively, as follows:

$$\frac{\partial \mathbf{p}}{\partial t} + \frac{\partial (\mathbf{p}\overline{u}_i)}{\partial x_i} = 0 \tag{1}$$

$$\frac{\partial(\rho\overline{u}_i)}{\partial t} + \frac{\partial(\rho\overline{u}_i\overline{u}_j)}{\partial x_j} = \frac{\partial\sigma_{ij}}{\partial x_j} - \frac{\partial\overline{\rho}}{\partial x_j} - \frac{\partial\tau_{ij}}{\partial x_j}$$
(2)

It should be noted that Equation (2) is the filtered form of the Navier-Stokes equations. The filtering is applied in order to separate the scales of turbulence, as a part of the LES turbulence modeling approach, into large scales and sub-filter or sub-grid scales. The turbulence model is required to account for the rotational air turbulence that is generated due to the tire (and groove) rotation, since it is not economical to directly solve for all the scales of turbulent motion for the problem considered. Thus,  $\tau_{ij}$  in Equation (2) is the subgrid-scale (SGS) stress tensor obtained as a result of the filtering of the nonlinear or convection term, which in turn requires closure in order to solve the governing equations. This is done using the Boussinesq hypothesis [15, 16].

$$\sigma_{ij} = \left[\mu \left(\frac{\partial \overline{u}_i}{\partial x_j} + \frac{\partial \overline{u}_j}{\partial x_i}\right)\right] - \frac{2}{3}\mu \frac{\partial \overline{u}_l}{\partial x_l} \delta_{ij} \tag{3}$$

$$\tau_{ij} - \frac{1}{3}\tau_{kk}\delta_{ij} = -2\mu_t \left(\overline{S}_{ij} - \frac{1}{3}\overline{S}_{kk}\delta_{ij}\right) \tag{4}$$

In Equation (4),  $\mu_t$  is the SGS turbulent viscosity. For the LES Smagorinsky model, the SGS turbulent viscosity is defined by,

$$\mu_t = \rho L_s^2 \left| \overline{S} \right| \tag{5}$$

Here,  $L_s$  is the SGS mixing length and  $|\overline{S}| = \sqrt{2\overline{S}_{ij}\overline{S}_{ij}}$ , for

$$\overline{S}_{ij} = \frac{1}{2} \left( \frac{\partial \overline{u}_i}{\partial x_j} + \frac{\partial \overline{u}_j}{\partial x_i} \right) \tag{6}$$

Therefore, although the change in temperature due to pressure changes are small, the filtered energy equation (Equation (7)) is solved as well as part of the compressible approach.

$$\frac{\partial(\rho \overline{h}_s)}{\partial t} + \frac{\partial(\rho \overline{u}_i \overline{h}_s)}{\partial x_j} - \frac{\partial \overline{p}}{\partial t} - \overline{u}_j \frac{\partial \overline{p}}{\partial x_i} - \frac{\partial}{\partial x_i} \left(\lambda \frac{\partial \overline{T}}{\partial x_i}\right) \\
= -\frac{\partial}{\partial x_j} \left[\rho \left(\overline{u_i h_s} - \overline{u}_i \overline{h}_s\right)\right]$$
(7)

Here,  $h_s$  and  $\lambda$  are the sensible enthalpy and thermal conductivity, respectively. The sub-grid enthalpy flux term on the right hand side of Equation (7) is approximated using the gradient hypothesis in order to provide closure to the energy equation.

$$\left[\rho\left(\overline{u_i h_s} - \overline{u}_i \overline{h}_s\right)\right] = -\frac{\mu_t}{P r_t} C_p \frac{\partial \overline{T}}{\partial x_j} \tag{8}$$

where,  $C_p$  is the specific heat for the fluid and  $Pr_t$  is the sub-grid Prandtl number. In addition, an ideal gas assumption, that accounts for the compressibility of air is used to couple the energy equation to the momentum equation.

#### 3.2 Acoustic model

An acoustic model needs to consider the propagation of acoustic waves originating at the near-field, with the far-field turbulence bearing no influence on the far-field acoustics [8]. Due to the ability of including the monopole, dipole as well as quadropole sources in the prediction of far-field acoustics, the Ffowcs-Williams and Hawkings (FW-H) model is used as the acoustic model in this paper. The FW-H model is an inhomogeneous wave equation, derived from the continuity and Navier-Stokes equations [17] and the solution for the far-field acoustic pressure, p', is obtained using Equation (9).

$$\frac{1}{a_0^2} \frac{\partial^2 p'}{\partial t^2} - \nabla^2 p' = \frac{\partial^2}{\partial x_i \partial x_j} \left\{ T_{ij} H(f) \right\} 
- \frac{\partial}{\partial x_i} \left[ \left\{ P_{ij} n_j + \rho u_i (u_n - v_n) \right\} \delta(f) \right] 
+ \frac{\partial}{\partial t} \left[ \left\{ \rho_0 v_n + \rho (u_n - v_n) \right\} \delta(f) \right]$$
(9)

In Equation (9),  $u_i$  is the fluid velocity in the  $x_i$  direction,  $u_n$  is the fluid velocity normal to surface, f = 0,  $v_i$  is the surface velocity in the  $x_i$  direction,  $v_n$  is the surface velocity normal to the surface,  $\delta(f)$  is the Dirac delta function and H(f) is the Heaviside function. The control surface around the near-field domain, which is used as the input for the acoustic model is represented by the surface f = 0.  $n_i$  is the normal vector in the direction of the exterior region,  $a_0$  is the far-field acoustic velocity. The Lighthill stress tensor  $T_{ij}$  is obtained using Equation (10) given by:

$$T_{ij} = \rho u_i u_j + P_{ij} - a_0^2 (\rho - \rho_0) \,\delta_{ij} \tag{10}$$

 $P_{ij}$  in Equations (9) and (10) is the compressive stress tensor, which for a Stokesian fluid is given by,

$$P_{ij} = p\delta_{ij} - \mu \left[ \frac{\partial u_i}{\partial x_i} + \frac{\partial u_j}{\partial x_i} - \frac{2}{3} \frac{\partial u_k}{\partial x_k} \delta_{ij} \right]$$
(11)

ANSYS Fluent has the capability of solving the CFD and FW-H model equations, simultaneously. This allows for a simultaneous solution of the near-field and far-field acoustics in the proposed model.

#### 3.3 Spectral analysis

The acoustic pressure obtained for the various receivers are analyzed using Fourier Transform tools. Specifically, the fast Fourier transform (FFT) technique available in Fluent is used to obtain the power spectral density (PSD) and sound

Table 1: Details for tire geometry and transverse grooves

Parameter	Value
Tire radius	332.2 mm
Tire width	200 mm
Number of grooves	2
Groove dimensions	$5 \text{ mm} \times 10 \text{ mm} \times 155.3 \text{ mm}$
Groove separation	5°
Operating velocity	40 km/hr
Groove deformation	22%

pressure level (SPL) from the pressure signals. The acoustic data is collected at all the receiver locations for a sampling frequency of 20 kHz. For the reference pressure,  $P_{ref} = 2 \times 10^{-5} Pa$ , the SPL is obtained from the PSD using the relation

$$SPL = 10log_{10} \left( \frac{PSD}{P_{ref}^2} \right) \tag{12}$$

The resulting SPL spectrum is converted into an A-Weighted SPL spectrum over a 1/3-Octave band by using the A-scale function. This kind of analysis closely approximates the frequency response of a human ear. In addition to PSD and SPL spectra, it is necessary to study the temporal variation of the acoustics in order to understand the causes of noise generation and isolate the different mechanisms. Therefore, the time-variation of acoustic energy is obtained using the short-time Fourier transform (STFT) algorithm in Matlab. STFT divides the signal into sections in time and applies a discrete Fourier transform to each of the sections. The result is a time-varying acoustic spectrum, also called a spectrogram.

# 4 Computational details

The computational details including a physical description of the problem are described in this section.

#### 4.1 Tire parameters

The details for the tire used in this study are listed in Table 1. The groove deformation value was obtained from the experimental study by [14]. The tire under consideration is of the size 215/60R16. The 3D shape of the tire is an undeformed cylinder with fillets to create lateral horn geometries. Two transverse grooves are considered in the simulation, separated by 5 deg in the circumferential direction. The grooves undergo a 22% by volume deformation at the tire/road interface, as the tire rotates at an operating velocity of 40 km/hr. The deformation is prescribed using a User Defined Function (UDF) at the boundaries of the grooves and mesh layering is done to deform the mesh inside the groove domains. The rotation of the tire is represented by velocity boundary conditions on the tire surface, while the groove rotations are incorporated using the sliding mesh technique. The velocity boundary condition is also prescribed to the ground surface in order to represent a rotating drum. The outer domain is considered to be large enough such that the pressure waves are either diffused or they permeate through without any reflection, using far-field boundary conditions. Ultimately, the computational considerations are made such that it represents an experimental setup in an anechoic chamber.

## 4.2 Computational mesh

Due to the complex nature of the geometry and need of consideration of various aspects of the fluid flow in the results, including rotational turbulence, the mesh generation process requires a lot of attention. For this study, an initial mesh is generated using tetrahedral elements growing from the tire surface in the near-field domain, while the far-field domain contains biased hexahedral elements. Since no ambient air velocity is considered, there is an absence of vortex shedding resulting from spanwise shear instabilities. Consequently, a symmetry boundary condition can be used and the computational domain can be halved, which helps to reduce the number of elements in the mesh. The initial computational mesh shown in Figure 2 still contains 16.5 million elements.

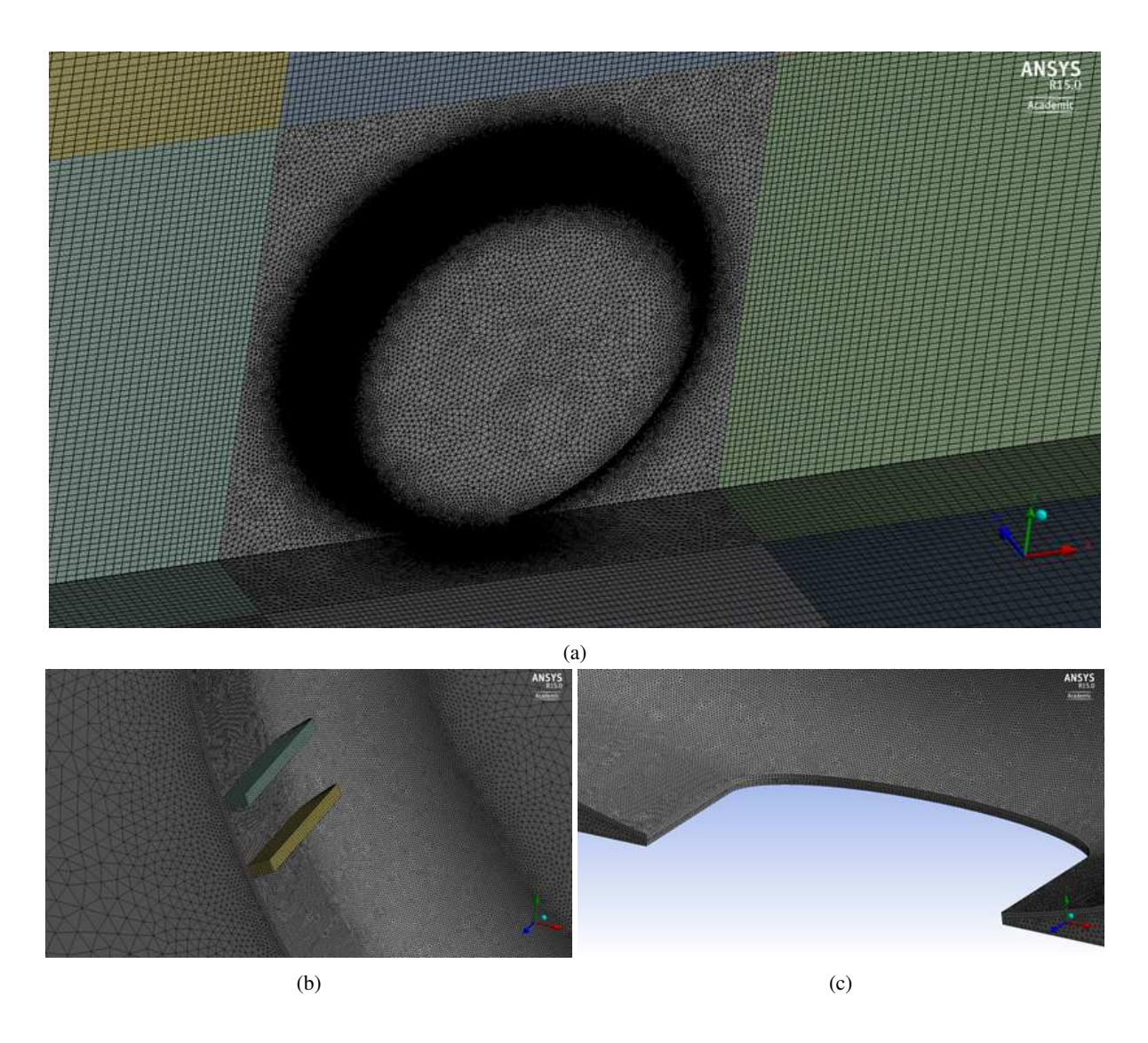


Fig. 2: Initial tetrahedral mesh (a) View from the symmetry plane, showing tetrahedral inner mesh and hexahedral outer mesh (b) Close-up view of two transverse grooves, meshed using hexahedral elements (c) Close-up view of contact patch generated by cutting off tangential surfaces.

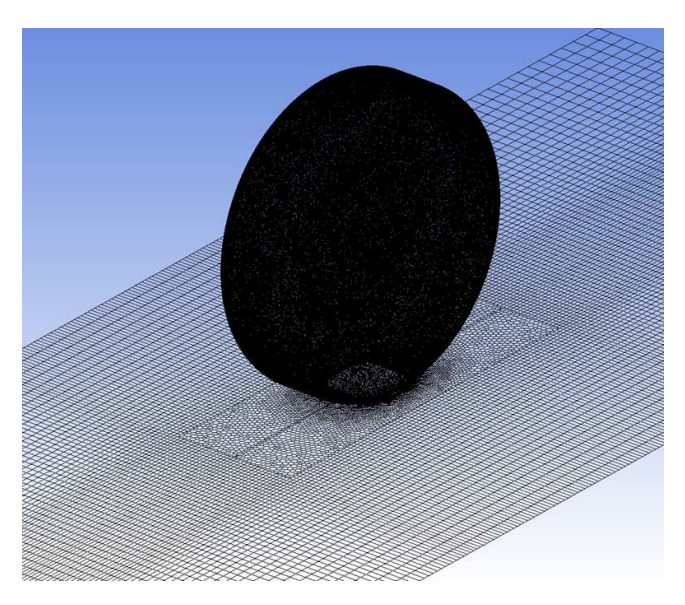


Fig. 3: Computational mesh showing polyhedral mesh in near-field domain and hexahedral mesh in outer domain

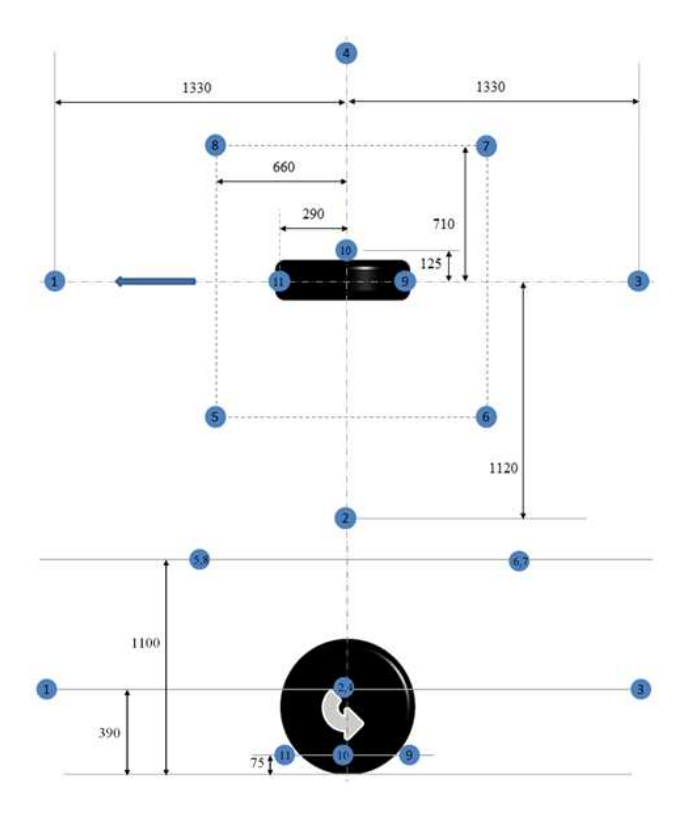


Fig. 4: Near-field and far-field receiver locations (in mm)

It can be seen from Figure 2b that the grooves contain hexahedral elements, while the tire surface is biased with prism layers close to the size of the elements inside the groove. This is done in order to facilitate an accurate interpolation between the tire surface and the domain interface of the grooves. Furthermore, it can be seen from Figure 2c, that a contact patch was been created by cutting-off the tangential contact between the tire and the ground surface. Since this is unavoidable in the creation of a valid mesh, this study takes advantage of this aspect, to create a contact patch. The length of the contact patch has been selected optimum mesh quality and number of computational elements. Furthermore, the cut-off also acts as a trigger to start the deformation of the grooves as they move into the contact patch. The custom UDF is written such that when the grooves are moving into the contact patch on the upstream side, they start deforming when the right-wall of the grooves (viewed from the symmetry plane) are in-line with the cut-off surface at the contact patch (Figure 2c) and they deform only until the left-wall of the grooves are in-line with the cut-off surface. Consequently, they move along the contact patch without any deformations and the process of deformation on the downstream side of the tire is the same as the upstream side. Finally, in order to reduce the computational expense further, the tetrahedral elements and prism layers are converted into polyhedral elements using the mesh conversion tool in Fluent, while the hexahedral elements remain unchanged. The resulting mesh contains approximately 4.1 million elements.

The computational solution is obtained using second order schemes for time and space. Second order upwind discretization schemes are used for all spatial terms except momentum, for which bounded central differencing is used due to the use of an LES model. The pressure-velocity coupling is accomplished using the PISO scheme. The time step size used is  $5 \times 10^{-6}$  s, which for an acoustic frequency of range 0.1-10 kHz, corresponds to 20 time steps per minimum acoustic wave period under consideration. Residuals of  $10^{-6}$  were obtained during convergence indicating that sufficient temporal resolution is achieved for an LES filtered computation of this nature.

#### 4.3 Acoustic receivers

It is necessary to place acoustic receivers both in the near-field and the far-field in order to obtain acoustic pressure data and analyze it. The receiver locations used in this study are similar to the ones used in the experimental study of Takami and Furukawa [14]. The locations are shown in Figure 4. Since a symmetry boundary condition is used, the acoustic nature of receivers 2, 5 and 6 are assumed to be similar to those of 4, 8 and 7, respectively, and the results for only one of the sides is shown in the paper. Furthermore, receivers 9, 10 and 11 are considered to be near-field receiver locations and the near-field domain has been made large enough to include the coordinate locations of these receivers. Consequently, the acoustic pressure data is obtained at these locations through the solution of the fluid dynamic equations. For the other locations, i.e. far-field receiver locations, the FW-H model is used to compute acoustic signals.

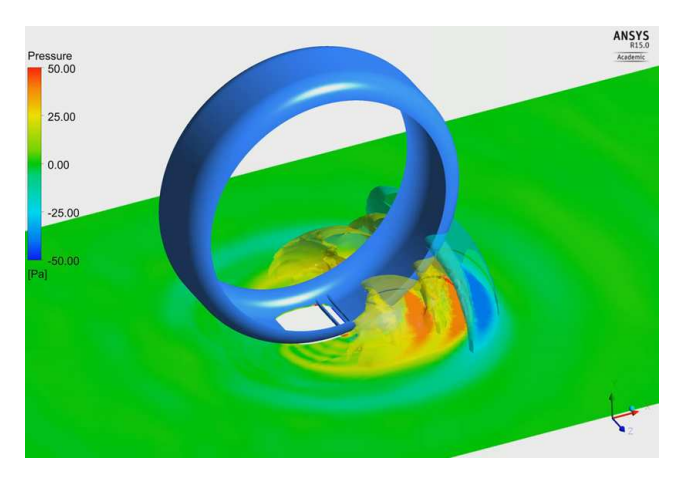


Fig. 5: Pressure iso-contours showing the propagation of pressure waves due to deformation of transverse grooves on the downstream side of the tire

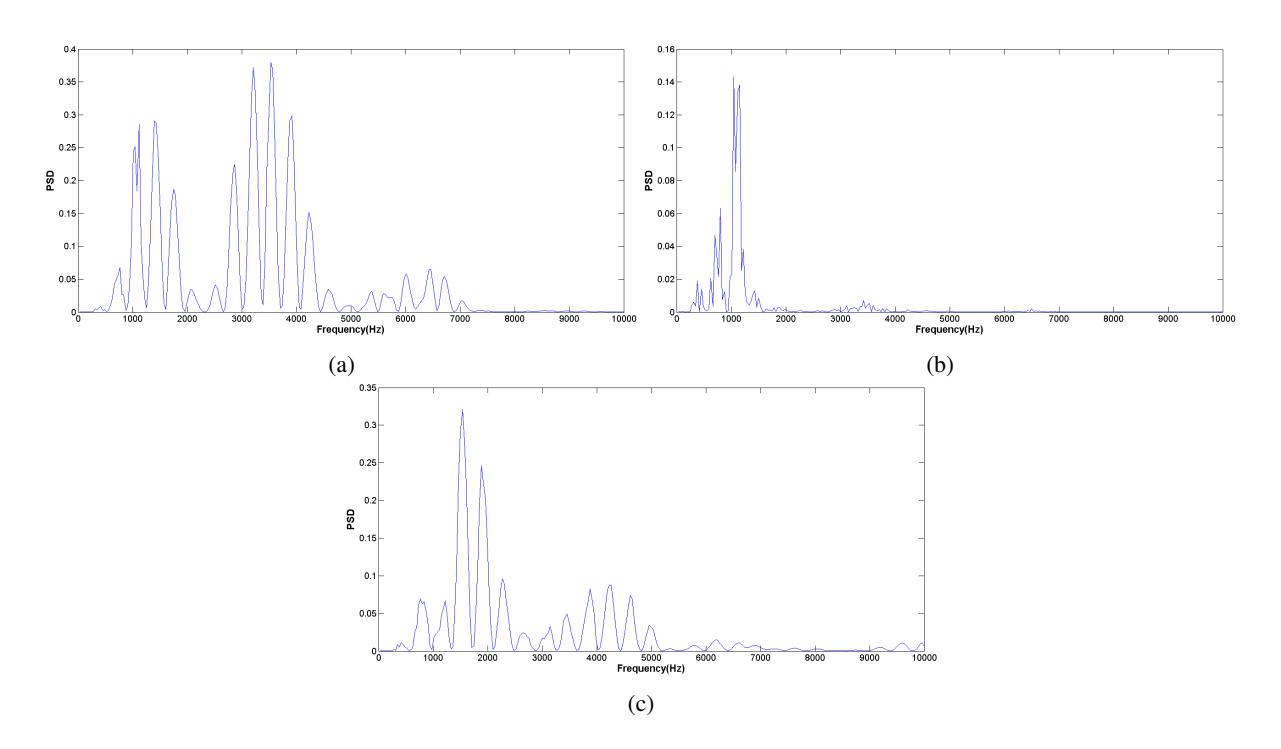


Fig. 6: Half PSD spectra for (a) Receiver-9 (b) Receiver-10 (c) Receiver-11.

### 5 Results and discussion

The initial condition of the transient computation corresponds to two grooves in a position fairly away from the contact patch in the upstream side of the tire, and the simulation is carried out until the grooves reach a position equidistant from the contact patch on the downstream side. Therefore, all pressure signals obtained at the receiver locations is due to the motion and deformation of the grooves at the contact patch, and the rotational turbulence generated, without any influence from the initial transients. Figure 5 shows an instant, where one of the grooves is in the contact patch (at stage IV), while the other is just moving out of the contact patch (at stage V), releasing acoustic pressure waves. The pressure iso-contours and the color map on the ground illustrate the 3D nature of the acoustic wave propagation.

#### 5.1 Near-field acoustics

The acoustic pressure signal at the near-field receivers 9,10 and 11 are used to study the near-field acoustic characteristics. The PSD spectrum is used to analyze the frequencies in which the acoustic energy is mostly concentrated and the spectra for the three receivers are shown in Figure 6.

While the grooves are moving along the contact patch, they can be considered as open pipes, since the only openings

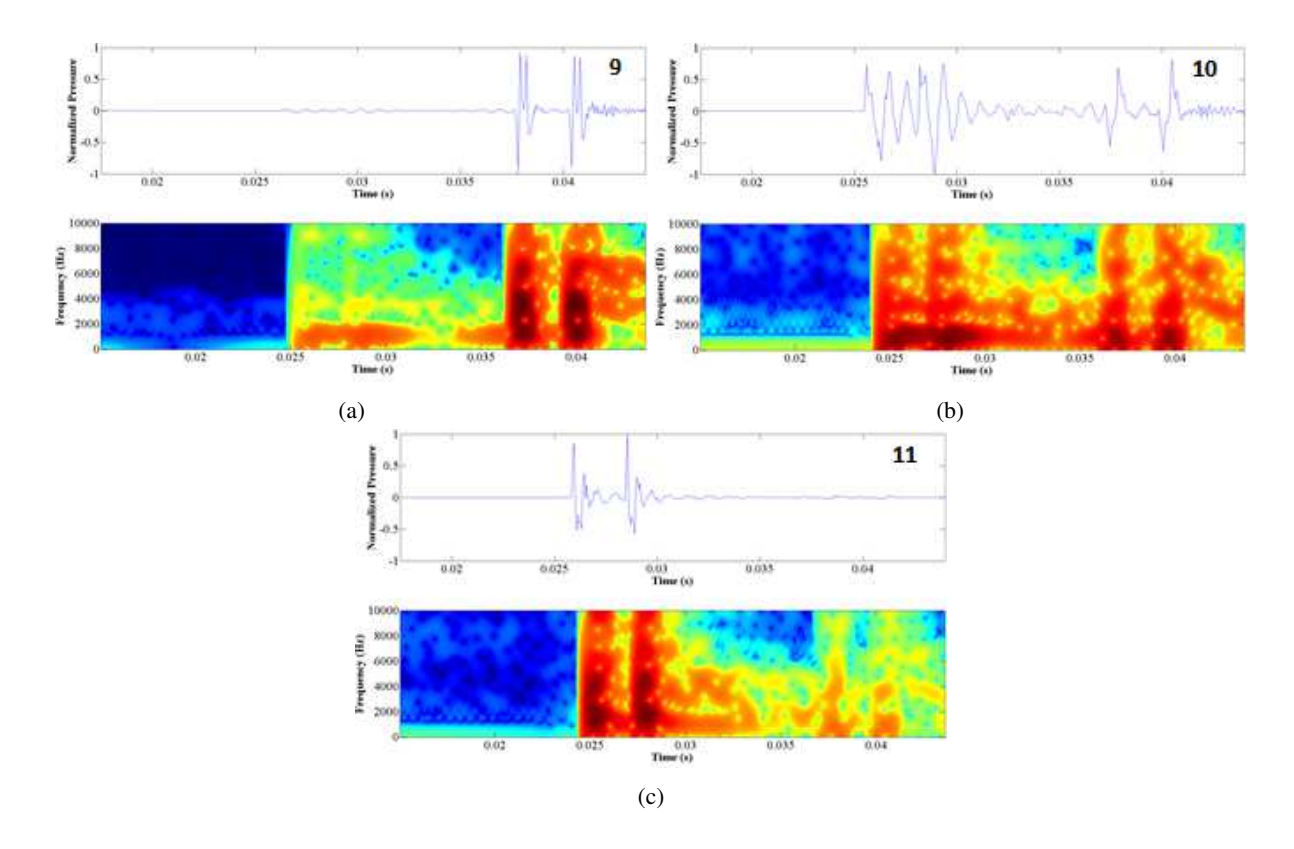


Fig. 7: Time variation of acoustic energy (spectrograms) for (a) Receiver-9 (b) Receiver-10 (c) Receiver-11.

are on the lateral sides. For an open pipe system, the resonance frequency is given by the relation,

$$f_R = \frac{c}{2l} \tag{13}$$

where, c = 340 m/s is the velocity of sound and l is the length of the open pipe. For the groove dimensions in Table 1, the pipe resonance frequency for the grooves resulted in  $f_R = 1.1$  kHz.

A concentration of acoustic energy in specific frequency bands can be seen from the spectra in Figure 6. These figures mainly illustrate the various frequencies of sound around the tire. At receiver-9 (Figure 6a), which is the downstream near-field location, it can be seen that there are comparable energy peaks for a number of frequency bands. The spectrum is able to capture the pipe resonance frequency (1.1 kHz) from the grooves as well as acoustics in higher frequencies. The spectrum at receiver-10 (Figure 6b), which is located close to the lateral horn geometry of the tire, shows the presence of acoustic energy corresponding to pipe resonance frequency, while there is an absence of higher frequency noise. It should be noted that there are no deformations taking place as the grooves move along the contact patch and thus, only pipe resonance frequency is captured at the receiver. The resonance frequency sound is low for receiver-11 (Figure 6c), and most of the acoustic energy is concentrated in the range of 1.6 to 2 kHz.

From the frequency spectra, it can be seen that the pipe resonance is captured in all three receivers, while there is a presence of higher frequency noise as well. In order to further study the nature of the acoustics at these receivers and understand further the high-frequency sound, spectrograms are generated, as shown in Figure 7. The colored bands are plotted along with the corresponding normalized pressure signals to illustrate the time-dependent nature of the sound at the receivers and isolate the source of the noise generated. Darker red colors in these spectrograms indicate higher acoustic energies for the corresponding frequencies on the Y-axis, at the corresponding time on the X-axis.

From Figure 7a, it can be seen that the acoustic energy captured is predominantly due to the motion of the grooves on the downstream side, since the pressure signals captured when the grooves are on the upstream side, are negligible. The spectrograms indicate that the acoustic energy is concentrated in frequency ranges similar to the ones seen in Figure 6a. For receiver-10, it can be seen from Figure 7b, that the pipe resonance frequencies are captured almost throughout the duration of motion of the grooves near and along the contact patch and there is minimal noise in other frequency ranges. The spectrogram for receiver-11 in Figure 7c shows that the acoustic energy generated is due to the motion and deformation of grooves in the upstream side as the pressure signal when the grooves are on the downstream side are negligible. By studying both the

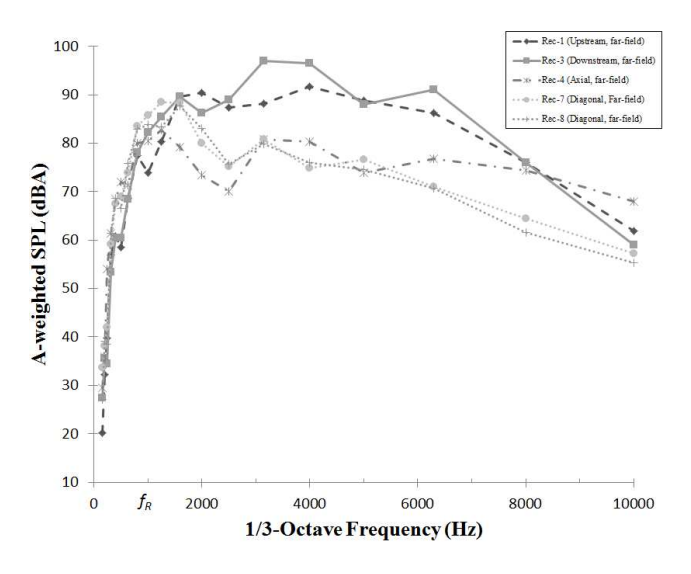


Fig. 8: dBA spectra for various far-field receivers

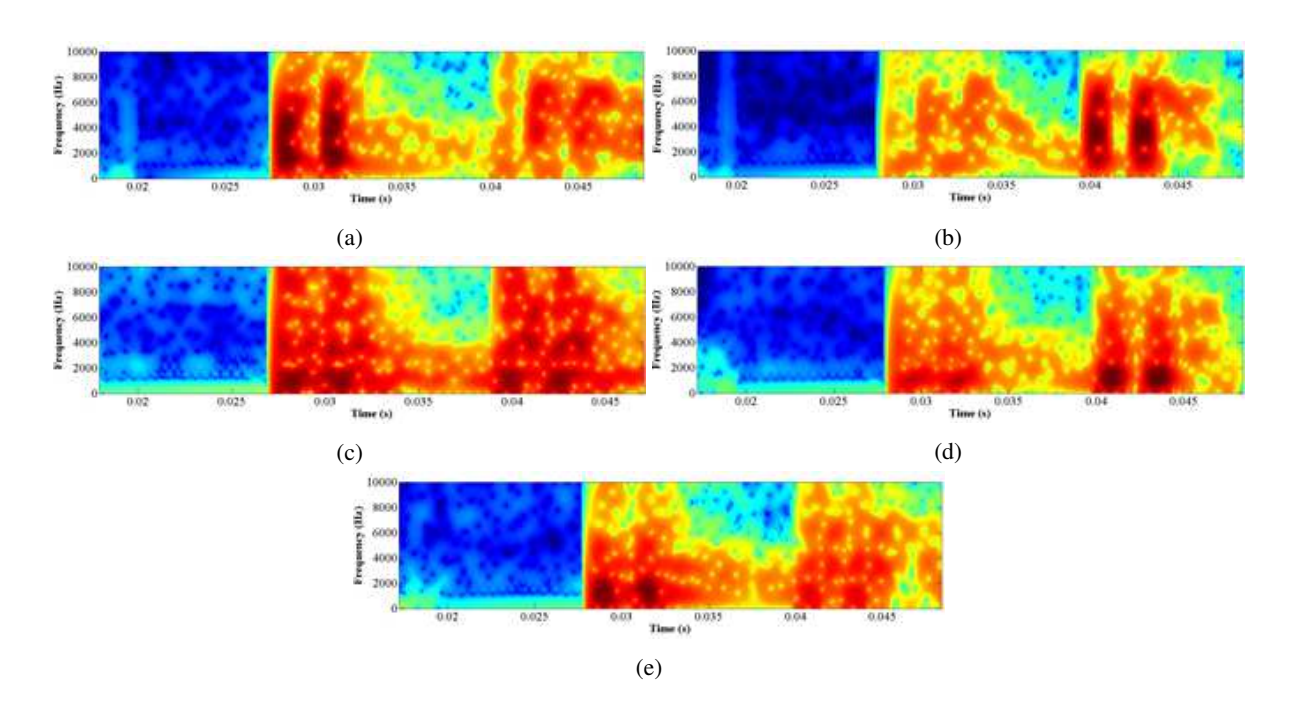


Fig. 9: Time variation of acoustic energy (spectrograms) for (a) Receiver-1 (b) Receiver-3 (c) Receiver-4 (d) Receiver-7 (e) Receiver-8.

frequency spectra in Figure 6 and the spectrograms in Figure 7, it can be concluded that the higher frequency acoustics are results of groove deformations.

## 5.2 Far-field acoustics

In this paper, the far-field characteristics are first analyzed using dBA vs. 1/3 octave frequency plots and also spectrograms for the far-field locations indicated in Figure 4. In addition, SPL polar plots are used to study the directive nature of the air pumping sound. The acoustic pressure signals at all the far-field receivers are obtained using the FW-H acoustic model.

#### 5.2.1 Far-field receivers

Figure 8 shows the SPL spectrum of the far-field receivers, obtained via spectral analysis of the far-field acoustic pressure signals. Different SPL peaks for the different receivers indicate that the nature of sound is different around the tire.

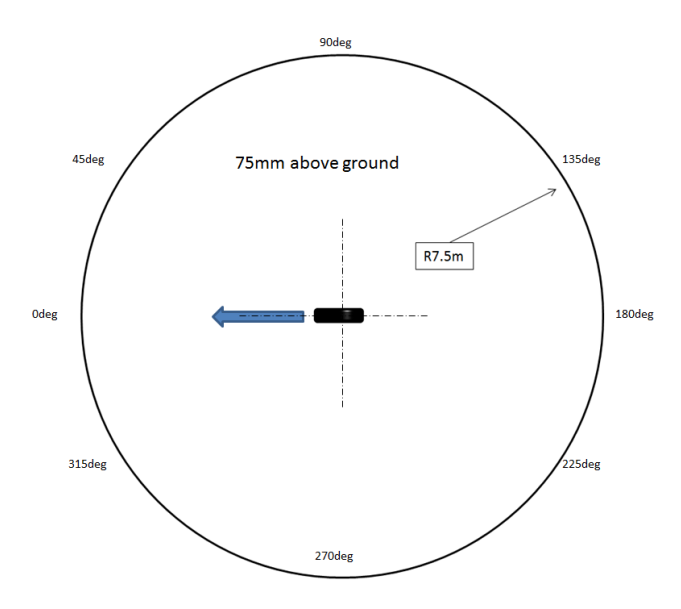


Fig. 10: Horizontal circular plane of radius 7.5 m for collection of wayside noise measurement data.

Furthermore, it can be seen that the receivers 1 (upstream) and 3 (downstream) are the loudest in the frequency range of 2-8 kHz while other receiver locations show peaks around the resonance frequency of 1.1 kHz. This is a similar trend to the near-field receiver locations, discussed in the section 5.1. Further information about the nature of the sound around the tire is obtained using the spectrograms in Figure 9. It can be seen that the nature of the spectrograms for the far-field receivers are similar to the near-field receivers on the corresponding sides of the tire. Therefore, a similar conclusion for the near-field and far-field receivers can be drawn that the higher frequency noise that is observed by analyzing the frequency spectra and spectrograms together is a result of groove deformations.

## 5.2.2 Far-field directivity

Additional information can be obtained about the nature of acoustics around the tire by analyzing the directive nature of sound on the far-field. A wayside noise measurement technique is commonly used experimentally to analyze far-field acoustics, where receiver locations are at a fixed distance of either 7.5 m or 15 m. In this paper, receivers are placed in a horizontal circle of radius 7.5 m and 75 mm above the ground surface and polar plots are generated to study the far-field directivity of the sound generated in the numerical model. The use of a computational technique in such predictions is advantageous due to the enhanced control of the environmental conditions resulting from the absence of any background noise in the simulations.

The resulting plots for 1/3 Octave frequencies between 0.8 kHz to 10 kHz are shown in Figure 11. The concentric circles in the plots represent A-weighted SPL values while the radial lines represent the polar locations. Since a symmetry boundary condition is used in the analysis, it is sufficient to place receivers between 0-180 deg, and the plot maybe mirrored to generate a 360 deg variation. The varying nature of the sound at different locations can be seen for each frequency from these polar plots. It can be seen that the variation of sound is pretty uniform up to 1.25 kHz, after which, the variation is more directive in nature as higher SPL values are observed on the upstream and downstream sides of the tire. Similar to the trend seen in Figure 8, the SPL values are low after 8 kHz. Furthermore, it can be seen that while the upstream and downstream sides have higher SPL values, the downstream side is the louder between two sides. This trend originates from the near-field spectra seen in Figure 6a, where it can be seen that there are various frequency bands of comparable energy levels, producing a larger overall sound level when compared to other near-field receivers.

# 5.3 Validation

A comprehensive experimental validation of the air-related noise generation mechanisms poses various challenges. Firstly, the background noise in an experimental setup does pollute the data to an extent. Also, it is very difficult to isolate the mechanical sources of noise from the aerodynamic sources in an experiment. Therefore, one mechanism is almost always present in the measurement of the other mechanism, and they cannot be easily isolated and studied. Hence, qualitative comparisons and mesh independence studies are used as a method of validation of the results presented here.

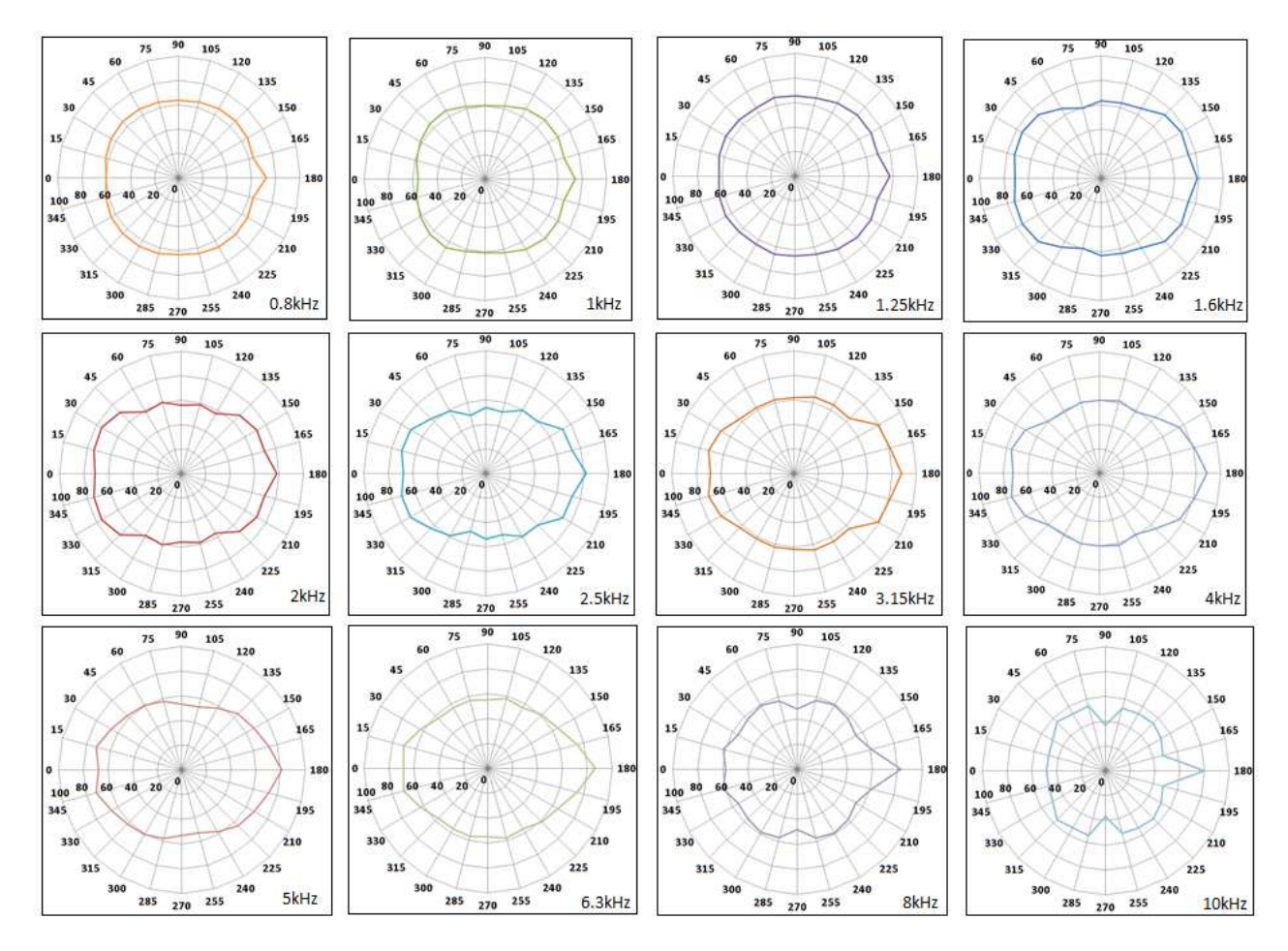


Fig. 11: Polar plots of SPL (dBA) for different 1/3 Octave frequency bands, at a location 7.5*m* from tire, concentric circles represent dBA.

## 5.3.1 Qualitative validation

It can be seen that the pipe resonance frequency obtained from Eq.(13) has been correctly predicted by the computation and it is visible in the frequency spectrum shown in Figures 6 and 8. Since only two transverse grooves are used in the simulations here, the impact noise which is visible in the analysis by [12], is absent here. However, it can be seen that the general range of frequency for air-pumping is consistent with [5,12]. From the polar plots shown in Figure 11, it can be seen that that sound has a directive nature starting from 1.6 kHz, with higher SPL values directly upstream and downstream of the tire. The reason for this could be the presence of larger horn geometries, thereby being consistent with [6]. Quantitatively, it can be seen that the SPL values vary between 60 dBA and 80 dBA, leading to a maximum variation of around 20 dBA around the tire. Attributing the magnifications to horn effect, this observation is consistent with the predictions in [6,7]. Additionally, the SPL values are higher on the downstream side, even though the rate and magnitude of volume change inside the grooves are same during compression and expansion. This observation can be attributed to the presence of a higher acoustic energy resulting from pipe resonance (See Figures 6a and 6c), and the Helmholtz resonance phenomenon [18,19]. It is caused when high pressure air which is trapped inside the grooves interact with and interrupt the suction of outside air although there is an increase in volume of the grooves. This phenomenon is also illustrated in a previous study [20].

#### 5.3.2 Mesh independence

To further validate the results, a mesh independence study is also carried out. The mesh element size used in the simulation is such that there are at least three elements per minimum acoustic wavelength. For a simulation without a mean flow, it is assumed that this resolution is sufficient. To ensure the mesh independence of the results, a coarser mesh with about 2.4 million elements after polyhedral conversion is used to carry out the calculation, with the same constraint that at least three elements are still present per minimum acoustic wavelength. The temporal resolution of the simulations remain unchanged assuming that it is fine enough to capture the frequency range of interest. Pressure signals are collected at the near-field receiver locations 9, 10 and 11. The normalized pressure for both meshes, obtained from the mesh independence study is shown in Figure 12. It can be seen that the pressure signals are similar in nature with very little deviation. Therefore,

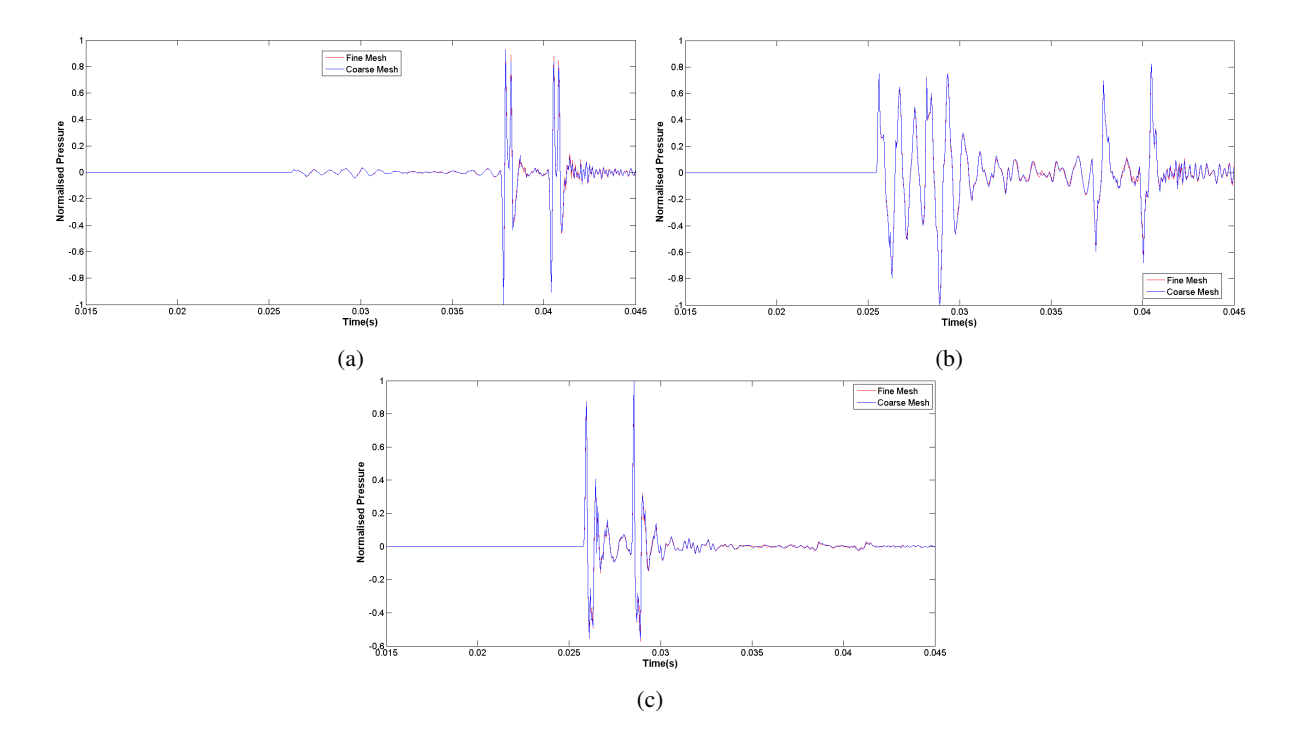


Fig. 12: Comparison of pressure signals for fine (red) and coarse (blue) mesh at (a) Receiver-9 (b) Receiver-10 (c) Receiver-11.

it is concluded that the mesh is fine enough to resolve all the frequencies considered in the simulation. Since the near-field domain is used to predict the far-field acoustics as well, validation of the near-filed pressure data is considered to be sufficient to validate the far-field acoustic data as well.

#### 6 Conclusion

In this paper, a new methodology is proposed to predict the 3-dimensional nature of the air-pumping noise generation mechanism in tires. Various near-field and far-field receivers are used to study the characteristics of the sound generated during air-pumping, and the various noise generation mechanisms that can be seen in the frequency spectra are studied. Furthermore, the directive nature of the sound is studied by generating polar plots from the computation.

It is found that the model is capable of incorporating various aerodynamic mechanisms that occur along with the airpumping noise generation in tires. It is shown that the frequency spectra, along with time-dependent spectrograms, can be used to isolate the causes of acoustics in the various frequency bands at various receiver locations. The horn effect is included in the model due to the horn geometry present in the 3D tire. The effect of the horn geometry can be illustrated through the polar plots. These plots show the directive nature of sound as it is amplified on the upstream and downstream sides and it can be observed that these amplifications vary in the range of 20 dBA around the tire. It can also be argued that the Helmholtz resonance mechanism has also been included in the model, since the motions in the model closely represent actual tire rotation and groove deformations using the sliding mesh technique. Also, it is observed that the sound is highest on the downstream side, where the effect of Helmholtz resonance is likely to be highest, although the volume changes in the grooves producing the sound is the same as for the upstream side. Furthermore, noise due to rotational turbulence is considered by the use of the LES turbulence model. The pipe resonance frequency, calculated to be around 1.1 kHz for the grooves considered, is also successfully captured by the computational model. Consequently, the results obtained show good qualitative agreement with previous studies, and the mesh independence study shows that the results presented are independent of the mesh.

As an extension to the model in future, a structural model can be coupled with the fluid model in order to more closely represent the deformation of the grooves and also include the deformation of the tire in the computational model. In doing so, a more complete computational model can potentially be used to incorporate not only aerodynamic, but also structural noise generation mechanisms in tires, and understand the interaction between these complicated processes.

## Acknowledgements

The authors would like the acknowledge the financial support from the Center for Tire Research (CenTiRe) during this project and also the industry members from CenTiRe for technical guidance and support. We are also grateful to Dr. Tomonari Furukawa and his research team from Virginia Tech. for his support in providing technical parameters from their tire noise experiments.

#### References

- [1] Iwao, K., and Yamazaki, I., 1996. "A study of the mechanism of tire/road noise". JSAE Review, 17, pp. 139–144.
- [2] Heckl, M., 1986. "Tyre noise generation". Wear, 113(1), pp. 157–170.
- [3] Gibbs, D., Iwasaki, R., Bernhard, R., Bledsoe, J., Carlson, D., Corbisier, C., Fults, K., Hearne Jr, T., McMullen, K., Roberts, J., et al., 2005. Quiet pavement systems in europe. Tech. Rep. FHWA-PL-05-011, U.S. Department of Transportation.
- [4] Sandberg, U., and Ejsmont, J., 2002. Tyre/Road Noise Reference Book. INFORMEX, Harg, SE-59040 Kisa, Sweden.
- [5] Eisenblaetter, J., Walsh, S., and Krylov, V., 2010. "Air-related mechanisms of noise generation by solid rubber tyres with cavities". *Applied Acoustics*, **71**, pp. 854–860.
- [6] Graf, R., Kuo, C.-Y., Dowling, A., and Graham, W., 2002. "On the horn effect of a tyre/road interface, part i: Experiment and computation". *Journal of Sound and Vibration*, **256**(3), pp. 417–431.
- [7] Ronneberger, K. S. D., and Schaaf, K., 1982. "Noise radiation from rolling tires-sound amplification by the horn effect". In Proceedings of Inter-Noise 1982.
- [8] Jiasheng, Y., 2013. "Tire-pavement noise simulation and analysis". PhD thesis, National University of Singapore.
- [9] Hayden, R., 1971. "Roadside noise from the interaction of a rolling tire with the road surface". *Proceedings of Purdue Noise Contr Conf*, pp. 62–67.
- [10] Gagen, M., 1999. "Novel acoustic sources from squeezed cavities in car tires". J. Acoust. Soc. Am., 106(2), pp. 794–801.
- [11] Gagen, M., 2000. "Nonlinear acoustic sources in squeezed car tyre cavities". *Noise & Vibration Worldwide*, **31**(4), pp. 9–19.
- [12] Kim, S., Jeong, W., Park, Y., and Lee, S., 2006. "Prediction method for tire air-pumping noise using a hybrid technique". *J. Acoust. Soc. Am.*, **119**(6), pp. 3799–3812.
- [13] Braun, M., Walsh, S., Horner, J., and Chuter, R., 2013. "Noise source characteristics in the iso 362 vehicle pass-by noise test: Literature review". *Applied Acoustics*, **74**, pp. 1241–1265.
- [14] Takami, K., and Furukawa, T., 2015. "Study of tire noise characteristics with high-resolution synchronous images". *Proceedings of EURONOISE*, pp. 2113–2118.
- [15] Garnier, E., Adams, N., and Sagaut, P., 2009. Large Eddy Simulation for Compressible Flows. Springer.
- [16] Pope, S. B., 2000. Turbulent flows. Cambridge university press.
- [17] ANSYS, INC., 2014. ANSYS Academic Research, Help System, ANSYS Fluent Users Guide, Release 15.0.7 ed.
- [18] Hamet, J., Deffayet, C., and Pallas, M., 1990. "Air pumping phenomena in road cavities". *Proceedings of INTROC*, **90**, pp. 19–29.
- [19] Nilsson, N., 1979. "Air resonant and vibrational radiation possible mechanisms for noise from cross-bar tires". *Proceedings of INTROC*, pp. 93–109.
- [20] Gautam, P., and Chandy, A., 2015. "Understanding tire acoustics through computational fluid dynamics (CFD) of grooves with deforming walls". In Internoise 2015/ASME NCAD Meeting.
- [21] Berckmans, D., Kindt, P., and Desmet, W., 2010. "Evaluation of substitution monopole models for tire noise sound synthesis". *Mechanical Systems and Signal Processing*, **24**, pp. 240–255.